Chapter 7
# Microscopic Features Characterizing Hydrogen Embrittlement

Fracture associated with plasticity proceeds by the nucleation of cracks or voids and their growth. This combination is crucial in fracture, and its evolution differs by situations like materials and applied stress states. Hydrogen degradation of macroscopic mechanical properties must originate in hydrogen effects in the microscopic process of fracture. Microscopic features are expected to exhibit more concretely the hydrogen functions in promoting failure.

7.1 Crack Nucleation Sites

Early works revealed striations on tensile-fractured surfaces of hydrogen-charged iron specimens [1]. Except for fatigue fractures, striated surfaces are not popular in fractographic features. Striations have been observed mostly for single-crystal and coarse-grain specimens. Figure 7.1 shows striations on the tensile-fracture surface of a hydrogen-charged 0.001% C iron single crystal [1]. The crack growth as a whole was in the [010] direction on a macroscopically (001) plane, but the actual growth of the crack front was in the <110> direction. Striations parallel to the crack front coincided with traces of {112} slip planes. Examinations of fine details utilizing scanning tunneling microscopy (STM) and mating of opposite fracture surfaces revealed the formation of fine voids at intersections of striations, as shown schematically in the lower part of Fig. 7.1. Crystallographic relations are consistent with the void formation originating in interactions of dislocations that move on intersecting slip planes.

Formerly, fine striations of about 1 μm spacing along {112} slip planes were reported to be associated with the slow crack growth macroscopically on {001} and in <110> directions for Fe-3%Si single-crystal specimens [2]. Acoustic emission (AE) measurements detected discontinuous crack growth in sustained-loading tests for fatigue-prenotched disk-shaped miniature compact tension specimens, which were

Fig. 7.1 Striations on the tensile-fracture surface of a hydrogen-charged iron single-crystal specimen. The lower illustration is a schematic STM view showing a microcrack formed at the intersection of striations (Terasaki et al. [1])
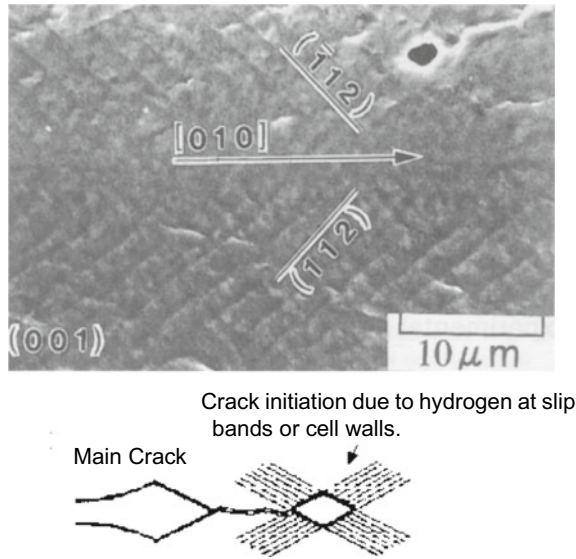

gaseous hydrogen charged and subjected loading parallel to <110> axis. The discontinuous steps were ascribed to intermittent cleavage fracture, but direct evidence for cleavage was not presented from crystallographic measurements.

The internal surface of hydrogen-induced cracks formed within coarse-grain polycrystalline Fe-3%Si specimens also exhibited fine striations and associated plasticity [3]. Internal cracks were initiated at non-metallic inclusions and propagated macroscopically on {100} cleavage planes associated with striations of an average spacing of 300 nm. More fine striations with a spacing of around 30 nm and a height of 15 nm were also observed. Transmission electron microscopy (TEM) revealed planar slip with an interplanar spacing of 15–30 nm that corresponded to the separation of fine striations. Electron backscatter diffraction (EBSD) patterns from regions within internal cracks were diffuse and indicated a substantial crystalline distortion.

The involvement of plasticity in hydrogen-induced crack growth was more explicitly observed for blisters in a bicrystal pure iron [4]. Hydrogen charging under a high hydrogen fugacity, i.e., by cathodic electrolysis in a 0.1 N H_2SO_4 solution with 10 mg/l As_2O_5 + 3 ml CS_2/l at a current density of 300 A/m^2, produced cracks without applying external stress. The cracks were parallel to variants of mostly {110} and partially to {112} instead of {001} in the case of Fe-3%Si specimens. Fracture surfaces, showing striations with planar segments and markings perpendicular to the advancing crack front, were common to Fe-3%Si specimens. Planar segments perpendicular to primary striations were also parallel to variants of slip planes. Striations noted in the above studies indicate a periodic crack advance, likely due to hydrogen diffusion, sequentially building up the hydrogen concentration at the crack front. The trace of the {112} slip plane along striations suggests the preparation of

Fig. 7.2 Cross-sectional view of the area beneath the fracture surface of a coarse-grain iron specimen tensile-fractured under hydrogen charging. The surface striations correspond to internal slip bands, and etch pits are formed along slip bands (Nagumo et al. [5])
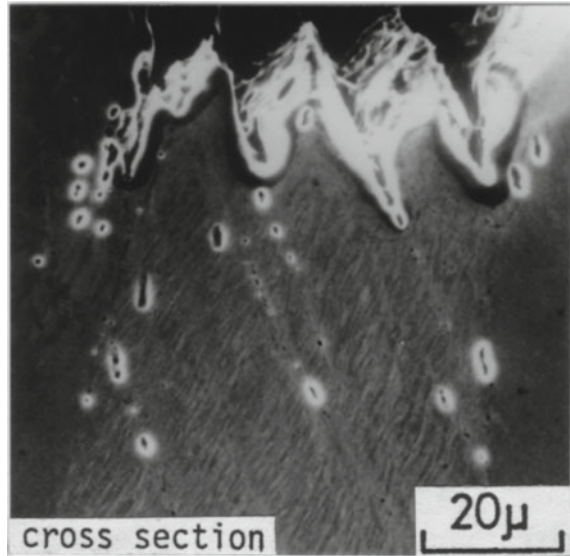

new cracks by activated dislocations. Direct evidence of the crack nucleation at sites of a high density of dislocations is shown in Fig. 7.2 [5].

More distinct and large striations were also observed. Figure 7.2 [5] shows a cross-section of a commercial pure iron specimen tensile fractured at room temperature under relatively mild hydrogen charging by cathodic electrolysis in a 3% NaCl aqueous solution at a current density of $100A/m^2$. The specimens of 5 mm in diameter had a bamboo structure, and fracture occurred after the onset of necking. The fracture surface exhibits coarse striations extending to internal deformation structures. A cross-sectional observation in Fig. 7.3 [5] revealed that the striations were on the extension of deformation bands in which etch pits and microvoids formed. Trace analyses confirmed the coincidence of the lamellae in Fig. 7.3 with {110} and {112} slip planes.

Deformation bands are regions where slip on the primary slip planes is hindered associated with the activation of secondary slip, thus causing there a high dislocation density and mutual interactions of dislocations [6]. A TEM observation near the fracture surface revealed dislocation cell structures with cell walls coincident with {112} traces [5]. Etch pits frequently observed in the deformation bands imply deterioration of crystallinity at the sites. Void nucleation is a natural consequence of intense strain localization, and the voids-link along deformation bands is a microvoid coalescence (MVC) process as general in ductile fracture.

Void nucleation sites resulting from interactions of high-density dislocations are not limited to deformation bands. Grain boundaries and interfaces of secondary particles, acting as barriers for dislocation slip, are viable sites, as described in the following.

Fig. 7.3 Etch pits and microvoids formed in deformation bands in a coarse-grain iron specimen tensile-fractured under hydrogen charging (Nagumo et al. [5])
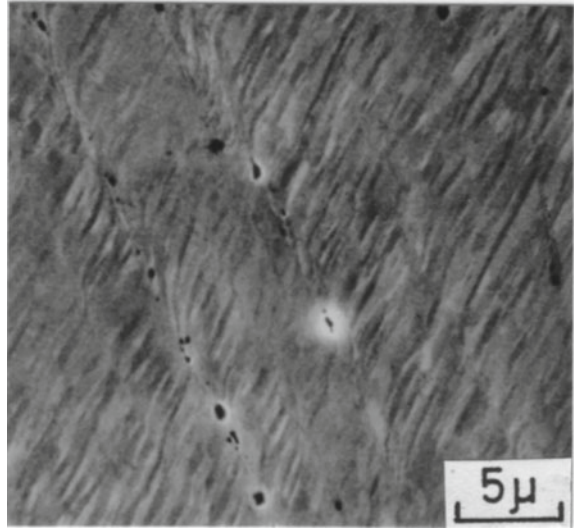
7.2   Fractographic Features

The fracture surface manifests the crack propagation path. Most of the energy dissipated in the crack propagation is due to plasticity, and its concern with the fracture surface is crucial to understand the mechanism of mechanistic degradation. Fracture surfaces of metallic materials are diverse depending on situations but are classified generally into a few elementary modes; cleavage, interface separation, and MVC. The fracture surface of hydrogen-degraded steel exhibits some characteristic features depending on microstructures, hydrogen concentration or fugacity, and stress states. Characteristic features in hydrogen embrittlement are to be examined along with the understanding of basic fracture modes.

7.2.1   Cleavage

Cleavage fracture is typical of brittle fracture of body-centered-cubic steel and is characterized by the transgranular crack propagation along {100} planes associated with river markings. In hydrogen embrittlement of steel, cleavage fracture is exceptional and appears when an incipient crack forms by the precipitation of molecular hydrogen of a high fugacity that satisfies the Griffith condition for an unstable crack extension. Cleavage fracture was observed for Fe-3%Si single crystals which were severely hydrogen charged either by cathodic electrolysis in a 4 vol.% H_2SO_4 + CS_2 + As_2O_3 solution at a current density of 160 A/m^2 or by quenching from a hydrogen atmosphere of 0.125 MPa at 973 ~ 1473 K [7]. The specimens were not

externally loaded, but arrays of decorated dislocations in the vicinity of cracks indicated plastic deformation associated with the discontinuous growth of cracks. On the other hand, under static loading under hydrogen charging, i.e., in sustained-loading delayed fracture tests, fracture surfaces exhibited many curved steps different from cleavage steps [8]. Cleavage fracture in hydrogen embrittlement was also observed on a tensile test of 0.014% C iron single crystal at room temperature under simultaneous hydrogen charging [1]. The tensile axis was along [001], and hydrogen charging was by cathodic electrolysis in poisoned 0.05N H_2SO_4 at a current density of over 30A/m^2. In that case, cleavage fracture with river markings occurred after the advance of the crack of striation-like appearance. The occurrence of cleavage might not be hydrogen effects.

7.2.2   Dimple Patterns

Dimple patterns typically characterize ductile fracture that proceeds with so-called microvoid coalescence (MVC). The size and shape of dimples are not uniform and are roughly classified into relatively large primary dimples and fine secondary ones. Second-phase particles, like non-metallic inclusions or precipitates, often locate in primary dimples, but fine secondary dimples are generally not associated with any particle. Activated dislocations are a most likely concern, and voids formed by the growth and coalescence of nanovoids resulting clustering of vacancies are a viable source of fine dimples.

Dimple patterns appear on hydrogen-assisted fracture surfaces of steel when a substantial ductility remains in degradation. Two cases are to be noticed for hydrogen effects on dimple formation. An increase in dimple size by hydrogen precharging was reported for tensile fracture of spheroidized near-eutectoid steels [9]. In that case, the diameters and spacing of carbides were less than or comparable to dimple size. Hydrogen precharging was under a high fugacity using cathodic electrolysis in 1 N H_2SO_4 poisoned by arsenic at a current density as large as 300A/m^2. High hydrogen fugacity of precipitated hydrogen should have caused decohesion of the interface between carbides and the surrounding matrix, promoting the void formation and the following growth. On the other hand, hydrogen generally reduces the size of secondary dimples. On a mixed mode I/III loading fracture toughness test of a high-purity Ni–Cr–Mo–V steel of lower bainitic structure of 855 MPa in tensile strength, hydrogen precharging at an equivalent hydrogen fugacity of 1.26 MPa at room temperature degraded the fracture toughness, associated with reduced dimple sizes compared with those of uncharged specimens [10].

The fracture surface at a three-point bending test of a mildly hydrogen-precharged low-carbon medium-strength steel plate exhibited patterns consisting of mostly primary and secondary dimples [11]. Hydrogen precharging enlarged primary dimples while reducing secondary dimples. The area fractions of dimples with different depth (h)/width (w) ratios are shown in Fig. 7.4 [11] for hydrogen precharged and uncharged specimens. Hydrogen precharging increased the area fraction of
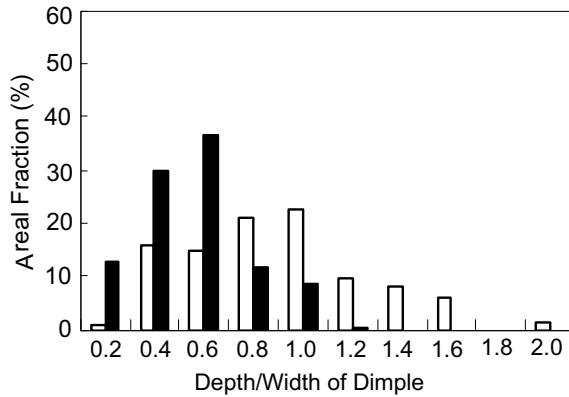
Fig. 7.4 Area fractions of dimples with different depth/width ratio on fracture surfaces of a low-carbon medium-strength steel subjected to a three-point bending test with/without hydrogen precharging. The open and filled bars indicate non-charged and hydrogen-charged specimens, respectively (Nagumo et al. [11])

shallow dimples ($h/w < 0.5$). It implies that hydrogen reduces the extent of plastic deformation to form dimples; thus, the energy dissipated during ductile crack propagation.

Shallowing of dimples generally characterizes moderate hydrogen degradation of steel. Examples are low alloyed steel in a three-point bending test [12] and Type 304 austenitic stainless steel in a tensile test [13]. An observation that suggested intimacy between dimple patterns and interface separation was tensile test results for as-quenched low-carbon martensitic steel [14]. An orientation relationship of the fracture surface that exhibited dimple patterns was parallel to $\{011\}_M$ planes which are also parallel to block and lath boundaries of martensite [14]. In that case, microcracks along prior austenite grain boundaries were present in areas far from the fracture surface. Hydrogen precharging was not mild, conducted by cathodic electrolysis in 1 N H_2SO_4 with As_2O_3 at a current density of 100A/m^2.

7.2.3 Quasi-cleavage

"Quasi-cleavage" is a term that broadly indicates fracture surfaces adequately flat with irregular markings but not specified to cleavage planes. Quasi-cleavage (QC) often appears in hydrogen embrittlement of steel, and the morphologies substantially differ by microstructures, specimen geometries, and hydrogen-charging conditions.

The fracture surface of low carbon-tempered martensitic steel (0.06C-5.9Ni-1.2Mn-0.7Cr-0.2Mo), subjected to three-point bending after hydrogen charging, exhibited irregular flaky patterns of about 10 μm in size [15]. The specimens were a fatigue-notched standard Charpy type, and hydrogen precharging was conducted by
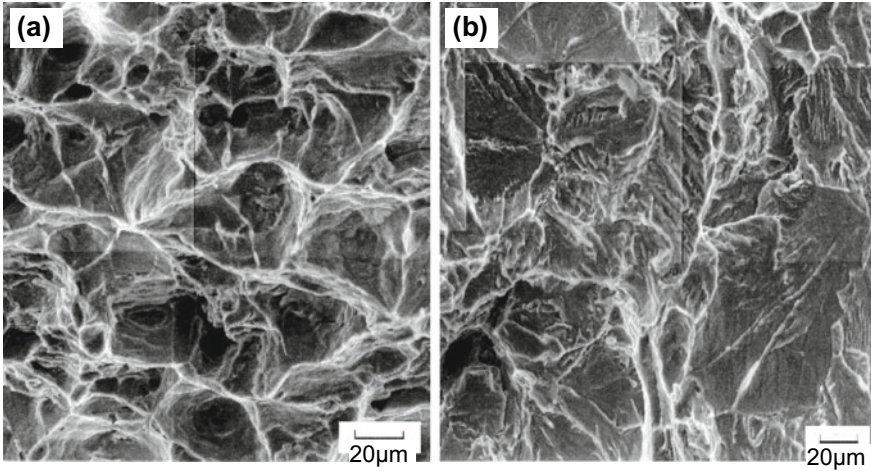
Fig. 7.5 Fracture surfaces of a low-carbon ferrite–pearlite steel subjected to three-point bending tests **(a)** without and **(b)** with hydrogen precharging. **(a)** dimple and **(b)** quasi-cleavage patterns. Hydrogen charging is conducted by cathodic electrolysis in 3% NaCl+ 3 g/lNH$_4$SCN at a current density of 5A/m^2 (Shimomura et al. [16])

cathodic electrolysis under a fairly high fugacity in poisoned 1 N H$_2$SO$_4$ at a current density of 10^3A/m^2. Scanning electron micrograph (SEM) revealed fine, lath-like features that correspond in dimension to martensite laths. From the shape of etch pits on the surface, their formation was on not cleavage {110} surfaces. Transmission electron microscopy (TEM) also revealed that the fracture surface was along martensite lath boundaries almost over its entire length. The lath boundaries are sites of high dislocation density. The observations also revealed many fine secondary cracks immediately beneath the fracture surface and their initiation at irregularities in the lath boundary, such as boundary intersections, steps, or foreign particles.

The intermediate range between ductile and brittle fracture is wide. QC locates in the intermediate range, and its morphology is diverse. QC surfaces like a premature dimple fracture often appear in hydrogen embrittled medium-strength steels and moderately embrittled high-strength steels. Figure 7.5 compares low-carbon ferrite–pearlite steel fracture surfaces subjected to three-point bending tests with and without hydrogen precharging [16]. The hydrogen charging was conducted under mild fugacity by cathodic electrolysis in 3% NaCl + 3 g/l NH$_4$SCN at a current density of 5A/m^2. After the onset of the stable crack, shown in Fig. 6.13, dimple patterns for the uncharged specimen changed to QC with irregular morphologies by hydrogen charging. Fine striations also appeared in the latter. Effects of hydrogen are reasonably ascribed to the cause of premature fracture before round-shape dimples form by substantial growth of voids. The reduced roughness of the fracture surface by hydrogen shown in Fig. 7.4 is consistent with the decrease in the crack growth resistance by hydrogen shown in Fig. 6.15 for low-carbon ferrite–pearlite steel of similar compositions.

QC surface in Fig. 7.5(b) is an extension of dimple fracture, but QC surface as an extension of intergranular fracture shows a significantly different morphology, as shown in Fig. 7.10. The latter usually appears in hydrogenated martensitic or bainitic high-strength steel. The morphologies manifest deformation microstructure to form the crack surface, naturally varying with steel microstructures.

Microstructural changes under the QC fracture surface were investigated using a focused ion beam (FIB) technique. Martin et al. examined the correspondence between fine topographic features and underlying microstructures of API X60 and X80 pipeline steel subjected to compact tension tests in high-pressure (5–100 MPa) hydrogen gas [17, 18]. The fracture surface exhibited different morphologies, and the surface with striations was referred to as QC. A topographic surface map showed that striations running approximately parallel to the crack direction were, in fact, ridges. At low magnifications, ridges on QC [17] and fine undulations on flat, featureless regions [19] correlated with intense and highly localized shear bands. In high magnifications, the undulation was composed of small ~50 nm rounded mounds with a high density of dislocation lines and loops immediately beneath the surface [18].

Similarly, the fracture surface of a medium-carbon high-strength martensitic steel, which was gaseous hydrogen charged and subjected to four-point bending tests, showed "flat" and "QC" features [19]. The maximum nominal bending stress decreased by hydrogen from 2415 to 501 MPa at room temperature. A high density of dislocations with localized slip bands was revealed beneath both "flat" and "QC" features, while the flat one was along prior austenite grain boundaries with destructed lath boundaries.

Martin et al. postulated that either near-surface relaxation after fracture or the underlying dislocation structures formed undulations and mounds on the fracture surface [18]. However, Lynch objected that mounds were possibly small, shallow dimples resulting from nanovoid coalescence during the fracture process [20]. Neeraji et al. carefully examined the fracture surfaces of hydrogen-precharged X65 and X80 line-pipe steel [21]. Evolution of a high dislocation density beneath QC facets was consistent with the observations by Martin et al., but mottled contrasts on the fracture surface were confirmed to be nanoscale dimples, 5 ~ 20 nm wide and 1 ~ 5 nm deep, of "valley-on-valley" type by mating halves of conjugate fracture surfaces. The findings indicate that nanovoid nucleation and linking, rather than the interface decohesion due to dislocation pileup, have occurred preceding the final fracture.

QC and striations that characterize fractographic features of hydrogen embrittlement of steel originate in intense strain localization at shear bands. Grain boundaries and interfaces of different phases, providing flat planes, are preferential sites for strain localization, i.e., QC, before substantial plastic deformation proceeds over the entire specimen. Shear localization promoting final fracture is described in Sects. 7.3.2 and 10.1.3 about the mechanism of hydrogen embrittlement.

7.2.4 Intergranular Fracture

In many cases, fracture surfaces of hydrogen-degraded high-strength martensitic steel exhibit morphologies that match prior austenite grains. The features have been assigned to intergranular (IG) crack propagation along prior austenite grain boundaries and have served as a basis for brittle fracture models of hydrogen embrittlement. The IG fracture is typical in the temper embrittlement of martensitic steel. As for hydrogen effects, step-cooling heat treatment of HY 130 (900 MPa in the yield stress) steel drastically reduced the threshold stress intensity K_{th} for no failure in edge-notched cantilever bend tests conducted in poisoned 0.1 N H_2SO_4 using pre-cracked specimens [22]. In unembrittled specimens, a slow crack growth started, showing fractographic features with some IG mode. The features soon shifted to a mixture of cleavage and MVC, then to full cleavage in the fast fracture region. On the other hand, the specimens embrittled by the step-cooling exhibited IG fracture from the crack initiation site through the slow and fast growth regions. Hydrogen favors IG fracture, and related results concerning the effects of impurity segregation in prior austenite grain boundaries on hydrogen embrittlement are described in Sect. 8.1.4a.

The impurity effects similar to temper embrittlement of martensitic steel led to the idea that IG fracture in hydrogen embrittlement is intergranular decohesion. However, the IG fracture surfaces are not quite smooth, and fine markings associated with plastic deformation are usually present. Gerberich et al. exhibited fracture surfaces mixed with IG, QC, and MVC regions for hydrogen-precharged AISI 4340 steel subjected to sustained-loading tests using compact tension specimens [23]. Hydrogen precharging was by cathodic electrolysis in poisoned 5% H_2SO_4 at a current density of 20A/m^2. The main fractographic features of specimens tempered at 503 K were IG and QC, and the fraction of IG increased by elevating test temperatures from 253 to 390 K. On IG facets, "brittle" striations appeared perpendicularly to the local crack growth direction. The striations occasionally accompanied some small tear ridges, and the spacing of striations was nearly coincident with the average martensite lath spacing of 1 µm.

A discussion on the crack growth behaviors at the test is described in Sect. 6.2.2.2. Gerberich et al. assumed that brittle striations were intermittent arrest lines of the advancing IG crack. The appearance of IG was less ductile than QC. However, the increase in the areal fraction of IG by elevating test temperatures was against an expected increase in ductility associated with the thermal activation of dislocations. A few oxysulfides observed on IG surfaces were not associated with ductile tears and were assigned to the origin of IG at elevated temperatures.

On the other hand, fractographic features of tempering at 723 K showed intermittent slow and fast-growing regions, accompanying mixtures of IG and MVC ductile rupture regions. The fraction of IG versus MVC was nearly fifty-fifty at room temperature. Ductile fingers or ligaments alternated in IG regions with a distance of about 200 µm. A series of second-phase particles were present on IG facets along ductile tearing striations. It was deduced that IG fracture started from the particles in regions 100 to 200 µm in extent and then destabilized the ligaments to cause tear by MVC.

Alteration of fracture morphologies associated with an extending crack concern the stress fields and microstructures in front of the crack.

Related information suggesting plasticity concerns was reported by Kameda according to X-ray diffraction line broadening on IG fracture surfaces [24]. Fracture surfaces of compact tension (CT) test specimens of hydrogen-precharged 3.5% Ni martensitic steel specimens showed IG fracture. Doping of phosphor and coarsening of prior austenite grain size reduced the threshold stress intensity and increased the crack growth rate. Rough and striped grain facets on fracture surfaces of undoped specimens became smoother and featureless by phosphor doping and grain coarsening. However, the {110} X-ray line was broader for the smooth surfaces than the rough surfaces. It indicates a substantial residual strain beneath the fracture surface, while plasticity is seemingly less on the fracture surface.

Different morphologies might have a common mechanism, as described in Chaps. 9–10. This aspect is stimulated by IG fracture not specific to steel and the presence of hydrogen. Fracture surfaces of ultra-high-strength 7075 aluminum alloys containing high Mg and Zn solutes were predominantly IG mode at fracture toughness tests, and a decrease in fracture toughness was accompanied by increasing amounts of IG fracture [25]. High magnifications of IG surfaces revealed very shallow dimples with fine particles (~0.1 μm). In situ observations of thin-foil specimens revealed void initiation at grain-boundary precipitates. It was postulated that constraints against deformation near grain boundaries induced the void initiation.

The evolution of IG fracture depends on the compositions of steel. Figure 7.6 shows fracture surfaces of medium-carbon Mn–Cr–Mo martensitic steel at slow-elongation rate tensile tests under simultaneous hydrogen charging [26]. The compositions of the steels were similar except Mn contents of 0.5, 1.0, and 1.5%. The specimens were plates of 2 mm in thickness and 10 mm in width without a notch. Simultaneous hydrogen charging was conducted by cathodic electrolysis in a 3% NaCl aqueous solution containing 0.5 g/l NH$_4$SCN at a current density of 5A/m^2. The tensile properties of the three steels were similar when hydrogen was absent, but a significant degradation appeared in hydrogen-charged specimens with increasing Mn contents.

Fractures under hydrogen charging were always initiated near the corner of the specimen, with IG fracture mode prevailing. Fine tear patterns were frequently observed on IG surfaces, but the surface was smoother for higher Mn contents. Chemical etching of the IG surface with saturated picral revealed tear markings along martensite lath boundaries. The average roughness of the fracture surface, measured using scanning laser microscopy, decreased with increasing Mn contents, as shown in Fig. 7.7 [26]. The roughness corresponds to the dissipated plastic energy on the crack growth. Lower roughness implies lower resistance to the crack advance, and the smooth IG surface can be a crack path with minimal energy dissipation.

The origin of energy dissipation in IG fracture is a subsequent issue. Martin et al. precisely examined dislocation activities regarding the IG fracture surface on Ni [27]. The material was a commercially pure Ni bar of 4 mm in diameter, thermally hydrogen charged in high-pressure hydrogen gas to about 2000 at ppm. The fracture surface by tensile straining at a strain rate of 4×10^{-4}/s was fully
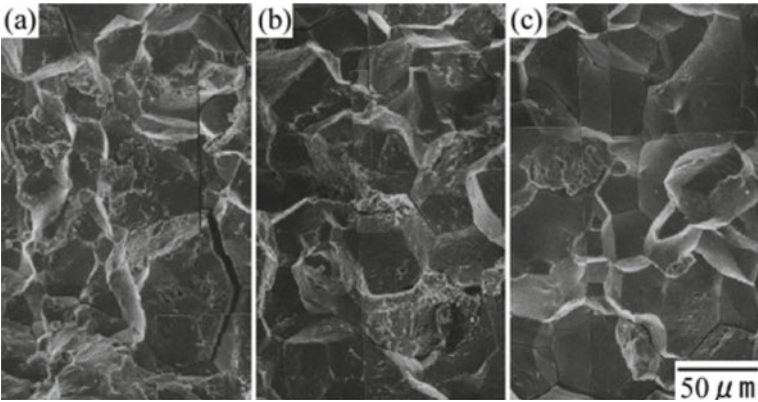
Fig. 7.6 Tensile-fracture surfaces of medium-carbon martensitic steels under hydrogen charging. Manganese contents: **(a)** 0.5, **(b)** 1.0, and **(c)** 1.5% (Nagumo et al. [26])
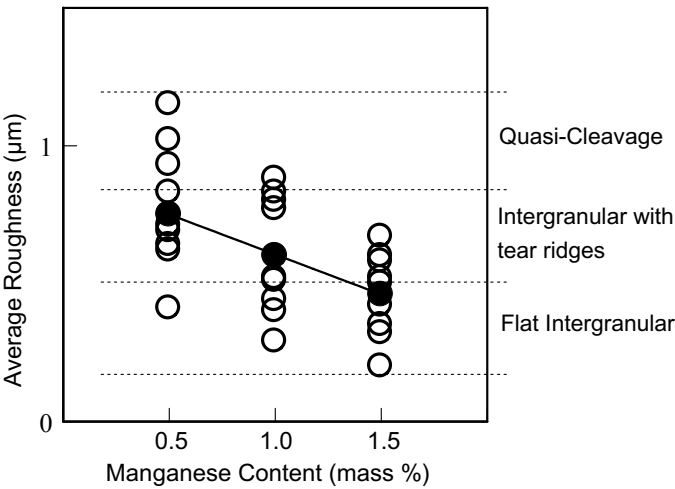

Fig. 7.7 Average roughness and patterns of fracture surfaces shown in Fig. 7.6 (Nagumo et al. [26])

intergranular, but high-resolution fractography exhibited slip traces about 1 μm apart. The microstructure immediately beneath the fracture surface consisted of a high density of dislocations, organized into cell structures on the order of 200 ~ 400 nm of the average cell size. High dislocation densities extended to 4 ~ 5 μm from the fracture surface. The existence of a grain boundary was not observed immediately beneath the surface, and the crack was supposed to *propagate in, not adjacent to, the grain boundary*. Similar results were also obtained for iron that contained 25.8 at. ppm hydrogen [28]. A seemingly flat IG fracture surface was highly distorted in a magnified sale.
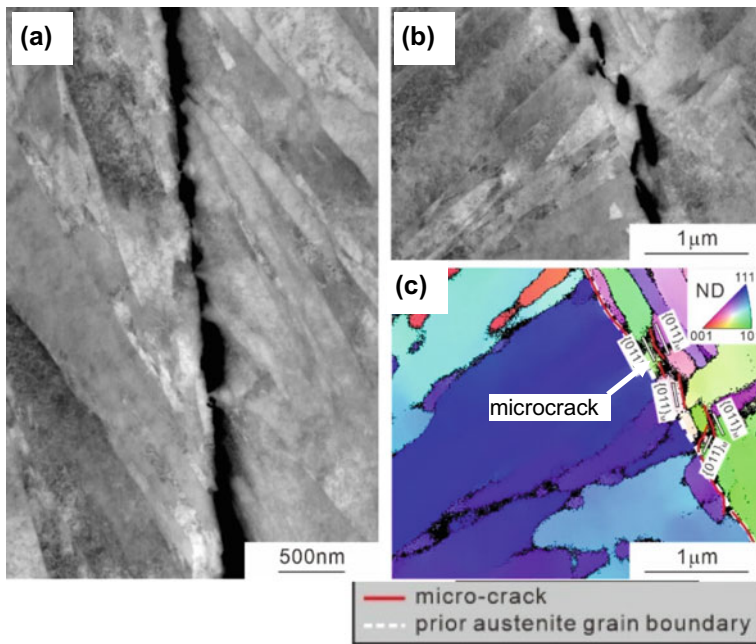
Fig. 7.8 (**a**), (**b**) Backscattering electron images and (**c**) Electron backscattering diffraction orientation map of the tensile-fractured Fe-0.2%C martensitic steel (Shibata et al. [29])

Shibata et al. examined a cross-section of a tensile-fractured specimen of as-quenched and hydrogen-precharged 0.2% C martensitic steel [29]. Figure 7.8(a) and (b) are backscattering electron (BSE) images of a microcrack present beneath the tensile-fracture surface, and Fig. 7.8(c) is the electron backscattering diffraction (EBSD) orientation map around the area (b). Several micro voids likely coalesced and propagated along {011} planes, slightly away from the prior austenite grain boundary.

7.2.5 Alteration of Fracture Morphology on Crack Extension

Fractography is a powerful tool to characterize the fracture type, but fractographic features are not uniform over the entire crack path. The stress-intensity factor K or J-integral, which represents the extent of stress fields in front of a crack, alters with the crack extension. The evolution of local deterioration of material that leads to fracture must vary with the crack extension.

In an early study, a pop-in crack introduced by wedge-loading of AISI 4340 steel specimens in 3.5% NaCl solution propagated under a freely corroding (stress corrosion cracking, SCC) or attached to Mg anode (hydrogen-assisted cracking, HAC)

condition [30]. The fracture surface showed transitions in a sequence of ductile dimple, QC, IG, and fast fracture. The test was under a constant displacement condition using a wedge-loading CT specimen, and the stress intensity (K) decreased during the crack extension. Beachem postulated that dissolved hydrogen-enhanced deformation and that K, the content of dissolved hydrogen c_H, and the microstructure determined the crack path. The combination of K and c_H at the crack tip varies with time.

Beachem proposed a qualitative diagram of the critical combination of K and c_H for each fracture mode [30]. According to the diagram, the fracture mode changes as MVC → QC → IG by either a decrease in K at a constant c_H or a decrease in c_H at a constant K. A change in K with the crack extension implies changes in the intensity and extent of the stress fields in front of the crack, affecting the activation of local plasticity. The diagram was experimental, and microscopic details of various fracture modes were not shown.

A change in the fracture mode of cracks from QC to IG was also observed for high-strength AISI 4340 and ASTM A490 steels subjected to constant-stress delayed fracture tests [31]. The steel was 1970 and 1700 MPa in tensile strength, respectively, and specimens were round or V-notched bars. Simultaneous hydrogen charging was by cathodic electrolysis in 1 N H_2SO_4 at a current density of 10–1000 A/m^2. The length of the QC region increased with decreasing notch sharpness and applied stress level. It was deduced that QC triggered IG and that the crucial process for starting delayed fracture was QC associated with plasticity even though the macroscopic fracture mode was brittle-like IG.

A subject of concern is the role of plasticity. Alternatively, a highly disordered microstructure was revealed on the fracture surface of a hydrogen-charged iron [32]. Plate specimens of a 0.06%C ferritic steel of 310 MPa in tensile strength were tensile fractured under concurrent cathodic hydrogen charging in a 3% NaCl+ 3 g/l NH$_4$SCN aqueous solution at a current density of 10 A/m^2. The hydrogen-charging condition was fairly mild, and the elongation to fracture was still as high as 19% in the presence of hydrogen. The fracture surface and the subsurface area were examined by transmission electron microscopy (TEM) using a focused ion beam (FIB) technique for the sample preparation.

The selected electron diffraction (SAD) from the fracture surface showed halo patterns, and the lattice image of the surface layer showed disordered distributions of atoms. The thickness of the layer was less than 1 μm, and the dislocation densities in neighboring areas were very high, forming cell structures. Similarly disordered, amorphous-like layers of about 50 nm in thickness were occasionally observed along dislocation cell walls at about 1 μm below the fracture surface. In the above experiments, many short cracks were present transverse to the tensile axis on the side surface of the fractured specimens. Similar to the subsurface area, a featureless zone existed in the crack front, as shown in Fig. 7.9 [32]. The SAD pattern in the insert showed halo rings similar to that at the subsurface, and the dark field image clearly showed the presence of amorphous-like structures in the crack front. The featureless zone of a few 100 nm in length was within the plastic zone. Amorphization just below the tensile-fracture surface was also reported for hydrogenated Type 316L steel [33].
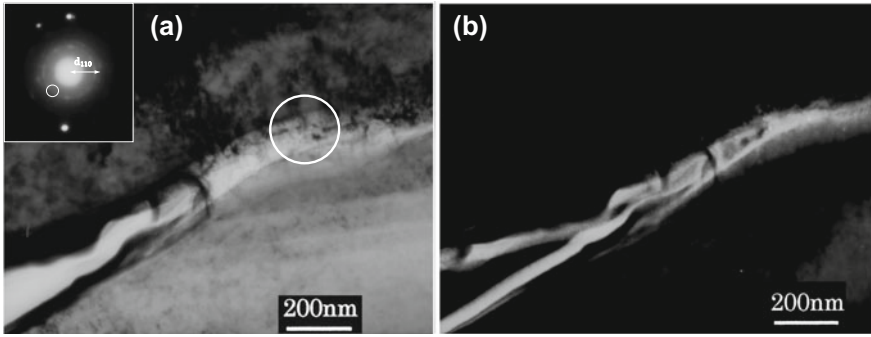
Fig. 7.9 (**a**) Featureless zone revealed by transmission electron microscopy in front of a small side crack formed on an iron specimen tensile-fractured under concurrent hydrogen charging. (**b**) The dark field image of the encircled area in (**a**) from a hallo ring in selected electron diffraction (Nagumo et al. [32])

Solid-state amorphization induced by heavy plastic deformation has been obtained by mechanical alloying. The mechanical property of amorphous metallic alloys is characterized by low strain-hardening that promotes strain localization and plastic instability. Hydrogen drastically reduces the ductility of amorphous metals accompanying volume expansion [34]. Heavily disordered microstructures shown in Fig. 7.9 are in accord with the high densities of vacancies described in Sect. 3.2.3.2 and are viable as the origin of reduced ductility. However, only limited observations have been reported on the amorphous phase formation at hydrogen embrittlement.

7.2.6   Fatigue Fracture

The fatigue crack growth (FCG) curves of some steels are shown in Figs. 6.20–6.23. Hydrogen generally accelerates the FCG rate in Stage II to Stage II' (the extended stage of Stage II after transient hydrogen acceleration), but the FCG rates at a stress-intensity range ΔK differ by steel and test conditions. Birenis et al. and Ogawa et al. examined the fracture surfaces of pure iron specimens subjected to fatigue tests in laboratory air and high-pressure hydrogen [35, 36]. Fatigue tests for fractographic examinations used a constant load amplitude (ΔP constant).

Figure 7.10 by Ogawa et al. [36, 37] compares fracture surfaces of pure iron in the air, (a) and (c), and 0.7 MPa hydrogen, (b) and (d), at ΔK of 12 MPa·m$^{1/2}$. ΔK of 12 MPa·m$^{1/2}$ was in Stage II in Fig. 6.21, before the onset of hydrogen acceleration in 0.7 MPa hydrogen. The FCG rates there were the same in the air and 0.7 MPa hydrogen, as shown in Fig. 6.21, but the fracture surfaces were substantially different. The surfaces are classified as QC. (Notice a broad range of the term "QC", referring to Fig. 7.5.) A high magnification shown in Fig. 7.10(c) in air exhibits QC covered with narrow ductile striations of the spacing more than one order of magnitude larger than
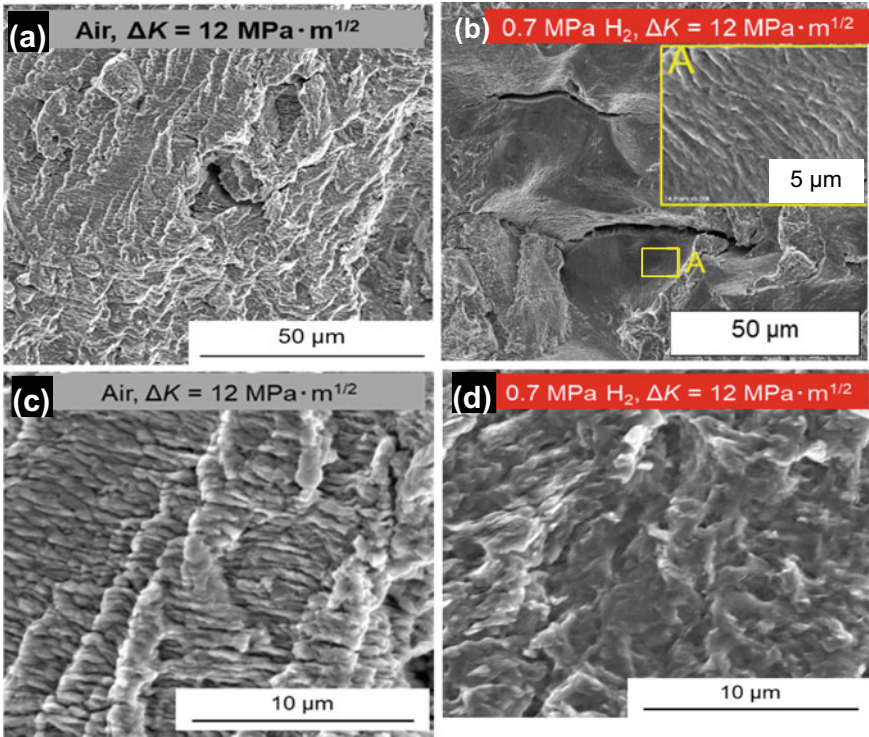
Fig. 7.10 Fatigue fracture surface of pure iron (**a**), (**c**) in air and (**b**), (**d**) in 0.7 MPa H$_2$ (Ogawa et al. [36, 37])

the apparent da/dN. On the other hand, Fig. 7.10(b) in 0.7 MPa hydrogen exhibits the fracture surface consisting of IG-like shallow facets mixed with ductile tear patterns and striations. The inset in Fig. 7.10(b) shows fine striations on an IG-like facet. A high magnification in Fig. 7.10(d) shows a part of irregular flaky units without distinct striations.

The hydrogen acceleration of the FCG rate was associated with change in the fractographic morphologies. An interesting result was that the area fractions of IG facets on the fracture surfaces were a function of ΔK values in the transition range, as shown in Fig. 7.11 [36]. The area fraction of IG decreases during the transition from Stage II to Stage II' and falls to almost zero at the late Stage II' in 0.7 and 20 MPa hydrogen. Accordingly, IG fracture per se is not the cause of a high FCG rate. For pure iron, the FCG rates in Stage II' were almost the same in 0.7 and 90 MPa hydrogen, and fracture surfaces of fairly flat and fine striations of irregular directions were similar.

On the other hand, for martensitic steel, the FCG rates in Stage II' in 90 MPa hydrogen differed by the strength, or the tempering temperature, of each steel, as shown in Fig. 6.22. At ΔK of 23 ~ 35 MPa·m$^{1/2}$, fracture surfaces were QC as a

Fig. 7.11 Area fraction of IG fracture surface of pure iron in high-pressure H2 as a function of ΔK (Ogawa et al. [36])
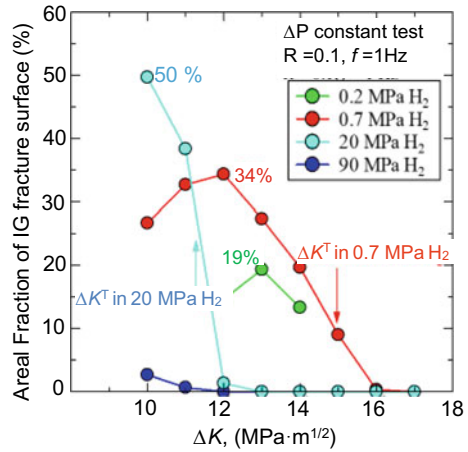
whole, but IG-like facets or cracks were present [38]. The area fraction of IG fracture surface at a constant-load amplitude test was about 0, 20, and 40%, respectively, for steel of 811, 921, and 1025 MPa of the tensile strength. High magnification of the IG-like facet was covered with fine slip-like patterns. The relation between FCG rates and fractographic features is not conclusive and is a matter for further examination.

7.3 Strain Localization

Strain localization is crucial in the void initiation and growth in plasticity-related fracture. Hydrogen effects on strain localization are vital for understanding the function of hydrogen in promoting fracture.

7.3.1 Surface Morphology

Fractographic features such as shallow dimples and QC in hydrogen embrittlement suggest that hydrogen suppresses the extension of plastic deformation on crack propagation. Hydrogen-enhanced strain localization has been reported mostly with slip morphology. Straightening, coarsening, and increasing the height of slip steps in the presence of hydrogen are general features on the fracture surfaces and side surfaces of tensile-fractured austenitic stainless steel foil specimens [39, 40].

On the other hand, the depression of surface reliefs around the advancing fatigue crack is shown in Fig. 6.24 for a bulky specimen of hydrogen-precharged Type 304 stainless steel [41]. Hydrogen was thermally precharged to about 90 mass ppm in high-pressure hydrogen, and the fatigue test was tension compression at a stress ratio

of −0.1 at the test frequency of 1.0 Hz. A small hole was drilled on the surface of specimens as the crack starter. The surface relief results from dislocation slip on different slip systems to accommodate stress relief on the crack advance.

The effect of hydrogen reasonably confines the extent of the plastic region involved in the crack advance. For austenitic stainless steel, the primary factor that promotes the planarity of slip is stacking fault energy. In fcc metals and alloys, the stacking fault energy plays a crucial role in plastic deformation associated with the ease of cross-slipping. Hydrogen reduces stacking fault energy, and reported reductions are from 18 ~ 15 mJ/m^2 to 12 mJ/m^2 by 12 mass ppm of hydrogen and from 34.2 mJ/m^2 to 27.7 mJ/m^2 under 5.3 kPa of hydrogen gas for a Type 304 austenitic steel [42] and a Type 310S austenitic steel [43], respectively. The effects of alloying elements on stacking fault energy in austenitic stainless steel were calculated by a first-principles calculation [44].

However, other types of steel also showed enhanced slip localization by hydrogen. Localized deformation around the advancing fatigue crack similar to Type 304 was observed for a high-strength Cr–Mo martensitic steel subjected to tension compression fatigue tests [45]. Specimens were hydrogen charged by immersion in 20% NH$_4$SCN aqueous solution at 313 K. Compared to hydrogen-uncharged specimens, the fatigue crack growth was straighter, with slip bands more concentrated near the crack front.

Effects of hydrogen on the morphology of slip bands were examined precisely for a 0.45% C steel with ferrite and pearlite structures subjected to rotational bending fatigue tests at 45 Hz using shallow-notched specimens hydrogen-precharged by immersion in 20% NH$_4$SCN aqueous solution at 313 K [46]. Slip band morphologies at the notch root, observed using a laser microscope for replicas of microstructures, were classified into three types, as illustrated schematically in Fig. 7.12 [46]. The fraction of ferrite grains of Type C with discrete localized slip bands was 49% in hydrogen-charged specimens after 6×10^5 fatigue cycles at 230 MPa, while Type C was not present in uncharged specimens. Also, about 20% of the crack initiation sites were along slip bands in hydrogen-charged specimens, while almost all were at grain boundaries in uncharged ones. The results demonstrated hydrogen-enhanced slip localization and the crack nucleation therein. Degassing by aging hydrogen-charged specimens at room temperature for 270 h substantially reduced the fraction of Type C grains after fatigue tests.

Intense slip bands act as crack initiation sites, as revealed in Fig. 7.2. Surface cracks at U-notch bend tests of spheroidized AISI 1090 steel specimens appeared at intense surface rumpling induced by slip bands [47]. The appearance was essentially the same between hydrogen-charged and uncharged specimens, but strain about a factor of two lower than uncharged ones brought about a similar surface roughness level or cracking in hydrogen-charged specimens [47]. A similar U-notch bend test was conducted for quenched-tempered AISI 4340 steel of 1.35 GPa in tensile strength with and without hydrogen precharging under a high hydrogen fugacity estimated to be 1GPa [48]. Hydrogen charging markedly reduced strain to fracture, and cracks nucleated internally in a mode I manner. The crack extension to the surface was along the characteristic slip path. Simultaneous hydrogen charging, instead of precharging,
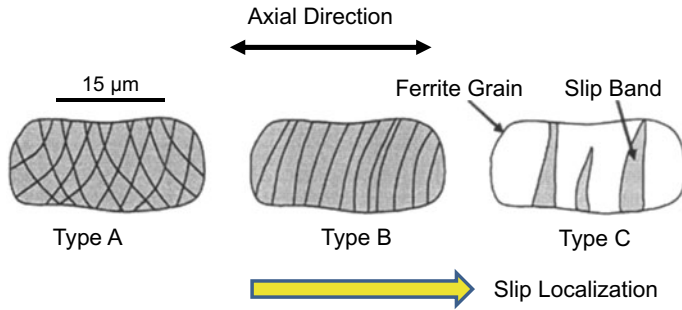
Fig. 7.12 Schematic illustrations of three types of slip bands at the notch root on 0.45% carbon ferrite–pearlite steel specimens subjected to rotational bending fatigue (Uyama et al. [46]. Reprinted with permission from John Wiley & Sons)

markedly promoted the crack nucleation reducing the plastic strain for the nucleation to zero.

7.3.2 Internal Structures

On examining the tensile-fracture surface of hydrogenated austenitic stainless steel, Ulmer et al. took notice of the continuity of steps on the fracture surface to internal slip bands and the crack formation along active slip bands [39], similar to Fig. 7.2 for pure iron. It suggests the extent of the region that concerns crack extension. Since hydrogen diffusivity in austenite is very low, the crack formation is hardly ascribed to the precipitation of molecular hydrogen during the test.

High-voltage electron microscopy (HVEM) revealed enhanced strain localization in the subsurface of fatigue cracks in Fe-2.6%Si single crystalline specimens [49]. The fatigue test was a sinusoidal tensile loading in hydrogen or helium gas of 0.58 MPa at a stress ratio of 0.1 and a test frequency of 1 Hz. The crack propagation was along the $(1\bar{1}0)$ plane in the [001] direction. Tests in hydrogen and helium gases exhibited remarkably different slip morphologies and crack outlines on cross-sections of specimens. In hydrogen, the crack tip was sharp, and the distribution of slip bands concentrated within 5 μm from the crack was consistent with the surface relief observed for austenitic steel [41]. Also noteworthy is that the immediate vicinity of the crack was severely deformed, while the crack outline was "brittle-like" straight. Slip bands were intermittently emitted from the crack tip, corresponding to the macroscopic crack growth rate.

The findings indicate that the crack advance is facilitated by highly localized strain at the crack tip prior to the extension of the plastic region that accompanies the macroscopic crack opening. However, which enhanced strain localization itself or the associated creation of defects or damage is the primary function of hydrogen in the crack advance is a matter to be examined further.

Fig. 7.13 GROD map, showing the rotation from the average crystal orientation, around fatigue crack in iron, in (a) air, (b) 0.7 MPa H_2, and (c) 20 MPa H_2. The arrowheads indicate the crack tip positions (Birenis et al. [35])
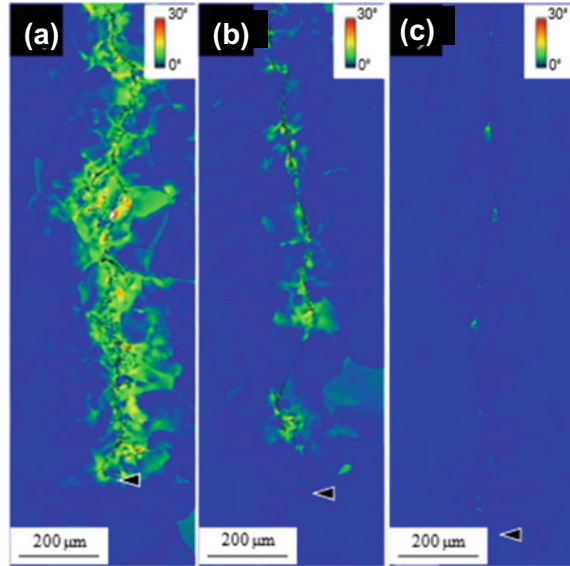

Birenis et al. examined a mid-thickness cross-section along the crack path of pure iron specimens subjected to fatigue tests in laboratory air and high-pressure hydrogen [35]. As a measure of the magnitude of local strain, Birenis et al. employed the grain reference orientation deviation (GROD), i.e., the rotation angle of each grain from the average crystal orientation in electron backscattering diffraction (EBSD) analysis. Figure 7.13 shows GROD maps along the cracks propagated in air and hydrogen gas in ΔK-constant fatigue tests at ΔK of 17 MPa· $m^{1/2}$ [36]. The crack runs from the upper to the lower side in the middle part of each map. The crack front is indicated by an arrow. Reduction in the width of the plastic zone, i.e., enhanced strain localization, by hydrogen is evident.

The fracture morphology of specimens at ΔK of 17 MPa· $m^{1/2}$ was generally QC according to Fig. 7.11, but the crack growth rates were in 90 MPa H_2 > 0.7 MPa H_2 > air. Hydrogen localizes plastic deformation in front of the crack, likely increasing the local density of damage. The involvement of plasticity in IG fracture, as a type of brittle fracture, is generally considered minor. However, in pure iron fatigue-fractured at ΔK of 10 MPa $m^{1/2}$ under 20 MPa hydrogen, **t**ransmission electron microscopy (TEM) of the region just beneath the IG fracture surface revealed dislocation cell structures, as shown in Fig. 7.14 [36]. The cell size was fine, less than 1 μm, at closer sites to the fracture surface, and nanovoids were occasionally observed, indicated by yellow arrows, within or close to cell walls.

Refined dislocation cell structures just beneath the fracture surface imply that hydrogen increases the energy density ahead of the crack tip. A high energy density and the associated deterioration of the material ahead of the crack tip must promote fracture at the crack tip. Which of the enhanced strain localization or the energy density is original is a vital issue for understanding the function of hydrogen to

Fig. 7.14 Transmission electron micrograph of an area beneath the fatigue-fracture surface of pure iron in 20 MPa H_2. Yellow arrows indicate nanovoids (Ogawa et al. [36])
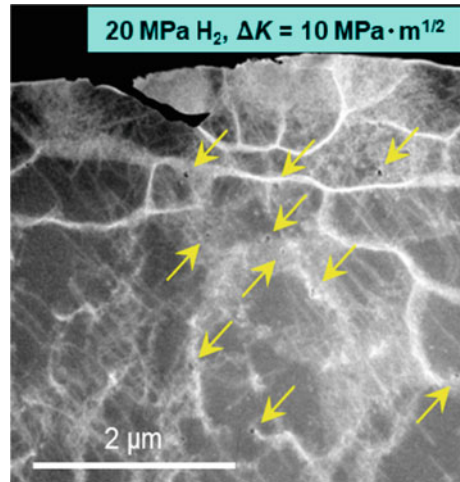
cause a premature fracture. Nanoscopic details of microstructures are requisite but not available at present.

Hydrogen effects on developing deformation microstructures were precisely analyzed by Okada et al. with tensile tests of low-carbon steel of ferrite microstructures [50]. A 0.1C-2Mn (mass%) steel sheet austenitized at 1173 K followed by furnace cooling was hydrogen charged by cathodic electrolysis in a 3% NaCl+ 3 g l^{-1} NH_4SCN aqueous solution at a current density of 5 A/m^2. On slow strain-rate tensile test of 8.3×10^{-6}/s, some specimens were unloaded at strain of 3%, 11.5%, 20%, and 24%, corresponding to the end of the Lüders deformation, the middle point of work hardening, the ultimate tensile strength, and prior to final rupture, respectively. For specimens at each deformation stage, the dislocation morphologies were characterized using scanning transmission electron microscopy (STEM) at an acceleration voltage of 200 kV.

At the initial stage of 3% strain, dislocations are linear while curved and tangled in the hydrogen-uncharged and hydrogen-charged specimens, respectively. At 20% strain, well-developed dislocation cell structures formed in both specimens without and with hydrogen charging. The cell is likely low energy dislocation structures, and the cell size tended to be smaller in the hydrogen-charged specimen than in the uncharged specimen. Figure 7.15 compares the statistical distributions of the cell size at 24% strain [50].

Further, STEM images with different diffraction vectors under two-beam conditions revealed the nature of dislocations. It was concluded that almost all of the straight dislocations in the uncharged specimen ($\varepsilon = 3\%$) had a significant screw component. The fraction of the screw component increased in the later stage of deformation in hydrogen-charged specimens, as shown in Fig. 7.16, while a certain number of dislocations that form cell boundaries are excluded [50]. Okada et al. deduced that these straight dislocations would be the origin of the tangled dislocation
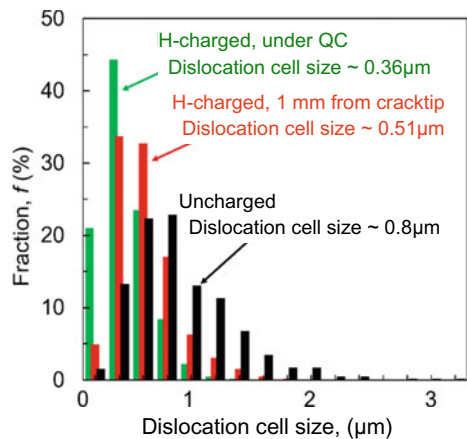
Fig. 7.15 Size distributions of dislocation cell near the crack tip in low-carbon ferritic steel tensile-strained to 24% with/without H-charging (Okada et al. [50])
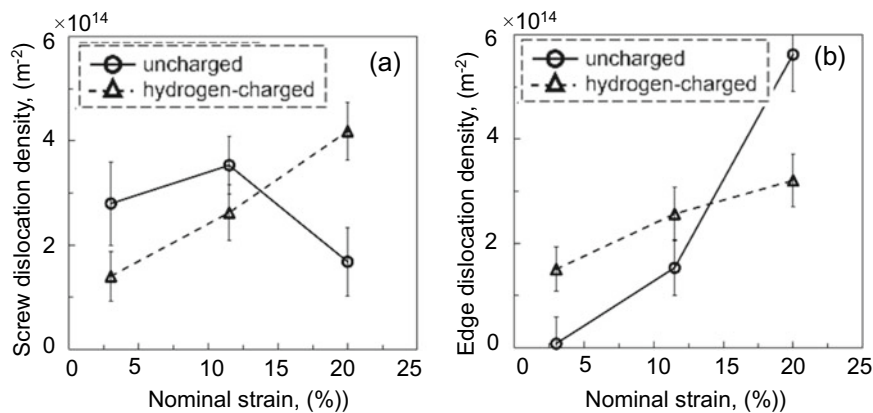

Fig. 7.16 Fractions of **(a)** screw and **(b)** edge dislocation densities of the uncharged (solid lines) and hydrogen-charged (broken lines) low-carbon steel as a function of nominal strain (Okada et al. [50])

morphology in the hydrogen-charged specimen: If hydrogen increased screw dislocation mobility, frequent cutting of screw dislocations would result in the tangled dislocation morphology. Okada et al. also deduced that jog-dragging by screw dislocations formed many vacancies on the {011} slip planes. In another aspect, an increase in the fraction of screw components is the reverse of a reducing fraction of edge components, a process generating many vacancies as described in Sect. 3.2.1.2. The proposed mechanisms of HE are described in Chaps. 9 and 10.

Methods to detect local strain distribution in materials are limited. Su et al. used in situ high-resolution X-ray tomography to observe internal strain and microvoids

during tensile straining of Al–Zn–Mg–Cu aluminum alloys [51]. The synchrotron X-ray beam in Spring-8 was used at 20 keV, and the effective pixel size of the detector was 0.5 μm. The Al–Zn–Mg–Cu alloys of 0.6 mm in thickness contained about 7 mass ppm hydrogen introduced on electrodischarge machining of specimens. The alloys contained fine precipitates, η_2 phase, and the internal strain was obtained from displacements of particles during straining. In the in situ tensile tests, the stress rise was intermittently stopped for an X-ray tomography scan, and the interruption caused stress relaxation while holding the displacement.

On the fracture surface, QC cracks initiated near the surface of the specimen and gradually transformed into dimple fractures on propagation. The strain map revealed a highly heterogeneous strain in all the strain components, especially along the fracture surface in the strain localization region. Obliquely aligned shear bands were a form, and a high hydrostatic strain concentration indicated volume expansion. Transmission electron microscopy (TEM) in the strain localization region revealed nanovoids that induce volume expansion, distinguishing from precipitates and dislocation pileups. Su et al. calculated the volume expansion using the theoretically estimated vacancy concentration and compared it with the measured volume expansion [51]. The calculated values in the localized flow region were nearly half of the measured values.

7.3.3 Plastic Instability

Plastic instability is the localization of plastic flow departing from a uniform deformation on stressing [52, 53]. Flow localization into a shear band appears as a void sheet linking [54]. Plastic instability evolves in uniaxial straining when the cross-section of a small portion of the specimen length reduces from that of the remainder, and the magnitude of the difference increases as straining proceeds. Plastic instability is a crucial process in ductile fracture, and its mechanistic significance for ductile fracture is described in Sect. 10.1.3.

The appearance of rugged surface shear bands at U-notch bend tests of spheroidized AISI 1090 steel indicated the onset of flow localization or plastic instability [47]. Hydrogen promoted the evolution of surface rumpling and reduced the critical strain for the onset of plastic instability well before the profuse void formation in bulk. Internal small crack nucleation following surface rumpling was along characteristic slip traces, as shown in Fig. 7.17 [47]. Criteria for the onset of plastic instability are derived from material constitutive relations. The critical principal notch surface strain observed at the onset of plastic instability was in good agreement with the calculated values for a U-notched bend specimen [47]. However, for a U-notched bend test of hydrogen-charged AISI 4340 steel, the critical notch-root strain at the crack initiation was nearly constant for three different notch-root radii of specimens [48]. Constitutive relations, such as yield stress and work-hardening rate, are generally insignificant as hydrogen effects. Then, it was deduced that hydrogen promoted plastic instability and that a combination of hydrogen concentration and total stress

Fig. 7.17 Schematic show of logarithmic spiral slip traces for circular notch root and the formation microcracks (Onyewuenyi et al. [47])
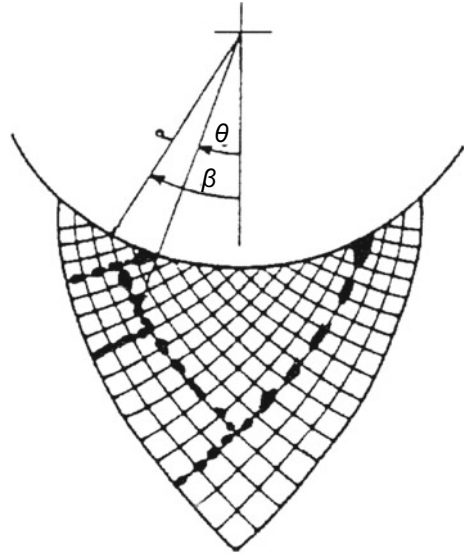
induced the crack nucleation within the plastic zone. The formation of a void sheet or its precursory crystalline disorder might be the cause of plastic instability.

A crack initially formed in the central part of the specimen propagated step-wise following a "void sheet" path. Link-up of microcrack with a void situated at the tip of the microcrack by shear was reported for spheroidized AISI 1520 steel bar specimens subjected to axisymmetric tension after hydrogen precharging [54]. In that case, second-phase particles are not ruled out as the crack initiation sites, but hydrogen promotes plastic instability and favors crack nucleation and propagation. The onset of plastic instability is due to sequential void nucleation and coalescence process. Hydrogen effects of decreasing fracture toughness on the mixed mode I/III loading tests, shown in Fig. 6.11, and the stable crack initiation from the pre-crack, shown in Fig. 6.9, are likely due to promoting plastic instability described in Sects. 10.1.3 and 10.4.

7.4 Damage Accumulation Precursory to Crack Nucleation

Hydrogen embrittlement attracts public attention when accidents in engineering service, such as delayed fracture of high-strength steel components or leak of sour oil/gas from pipes, happen. Most studies so far have remarked on the onset and growth of cracks. However, the degradation of materials in stages preceding the onset of fracture is crucial, and the effects of hydrogen on the creation of damage in materials are critical subjects. The term "damage" in engineering often addresses

flaws such as cracks or voids, but it is used widely in the present context, addressing crystalline deterioration far below the visual scale.

7.4.1 Damage Precursory to Crack Initiation

7.4.1.1 Microscopic Observations

An early study detected local lattice distortion as smearing of X-ray Kossel lines around hydrogen-induced cracks for pure iron single crystal [55]. Cathodic hydrogen charging at a current density of 300A/m^2 without external stress produced internal cracks of 50–75 μm in size, accompanying lattice distortion localized within 100 μm from the cracks. However, distorted absorption conics (Kossel lines) were also observed in regions where cracking had not yet occurred. Broadening of X-ray diffraction line width, associated with hydrogen charging, was also observed for mild steel specimen cathodically hydrogen charged in poisoned 0.1 N H_2SO_4 at a current density of 10^3 A/m^2, a high hydrogen fugacity [56]. The line broadening remained during exposure of specimens at room temperature but decreased about 25% at 473 K and almost disappeared at 673 K. Hydrogen trapped in elastic fields is ready to diffuse out at room temperature. However, its dissociation from strong traps like vacancies occurs at elevated temperatures, as described in Sect. 3.2.1. The aging behaviors implied that the line broadening was not due to elastic strain around hydrogen atoms but to plastic deformation induced on hydrogen charging. The aging behaviors are consistent with TDA results of Figs. 3.4(b) and 3.14, which imply the presence of vacancy-type defects created by plastic straining.

Effects of hydrogen on inducing lattice distortion are prominent when plastic straining has been or is simultaneously applied to the specimen. The image quality (IQ) in EBSD analysis represents the crystallinity of the diffracting area, and dark contrast results from lattice distortion. Figure 7.18 [13] shows IQ maps of hydrogen-charged Type 304 austenitic stainless steel given a tensile strain of 5% or 24%. The maps show lattice distortion with increasing strain more pronounced in regions close to grain boundaries than in bulk. The average strain separately obtained from Kernel average misorientation (KAM) maps, a measure of the orientation difference between neighboring areas, was reasonably lower for the specimen strained to 5% than that for 24%. However, a preferential strain localization appeared in hydrogen-charged Type 304 steel at a strain as low as 5% [13]. Annealing twins were often observed within grains, as indicated by arrows in Fig. 7.18, and twin boundaries tended to become blurred with increasing strain, implying distortion of areas near the interface of twin bands.

Nibur et al. examined fractographic features and deformation microstructures of 21Cr-6Ni-9Mn austenitic stainless steel specimens subjected to a compact tension test after thermal hydrogen precharging [57]. The features somewhat differed by ferrite volume contents in the material, but shallow, non-equiaxed dimples and flat facets with limited plasticity characterized the effects of hydrogen precharging.

Fig. 7.18 Image quality (IQ) maps of EBSD for hydrogen-charged Type 304 austenitic stainless steels tensile-strained to **(a)** 5% and **(b)** 24%. Arrows indicate annealing twin boundaries (Hatano et al. [13])
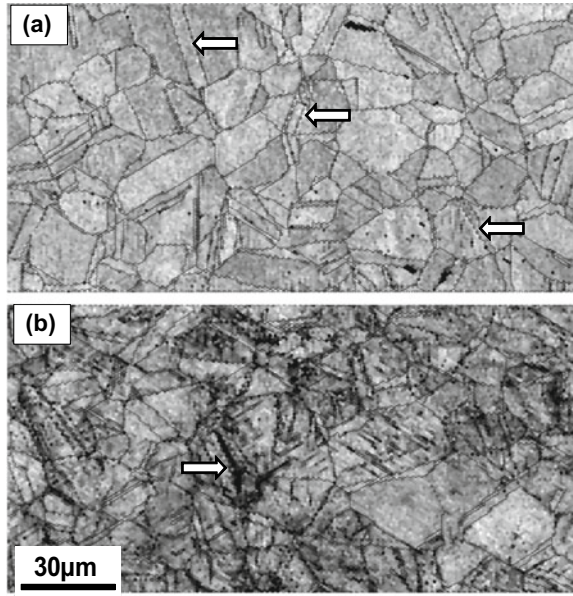
Examinations of cross-sections revealed the primary void nucleation at deformation band intersections, and concentrated microvoids were present along a continuous obstacle, such as another deformation band. Fine, elongated dimples covered relatively large facets. Microcracks were revealed along annealing twin boundaries at intersection points with deformation bands in the annealed material. The observations are consistent with the formation of small cracks at the intersection of slip bands shown in Fig. 7.1 for pure iron and the void nucleation in deformation bands shown in Figs 7.2 and 7.3 for ferritic steel. Fractographic features and deformation microstructures of austenitic stainless steels are further described in Sects. 8.3.3 and 8.3.4.

Nibur et al. postulated that hydrogen-enhanced localized plasticity (HELP) causes strain discontinuities at obstacles and void nucleation. However, deterioration of crystallinity along twin boundaries shown in Fig. 7.18 for Type 304 steel is viable as the precursor of void nucleation. An issue is again which of the enhanced plasticity or the strain-induced generation of vacancies (HESIV) has hegemony for the function of hydrogen in promoting failure.

### 7.4.1.2   Detecting Lattice Defects

Lattice defects creation during rotational bending fatigue tests of hydrogenated high-strength Si–Cr steel is shown in Fig. 6.18, using TDA of hydrogen introduced as the tracer of defects. Samples of the tracer-hydrogen contents in Fig. 6.18 are portions close to the fracture surfaces. The fatigue-cycle dependence of the density of lattice

defects was examined using the same test method for two martensitic steels, i.e., a high-strength Si–Cr steel bar designed for spring and a PC steel bar for prestressing tendon [58]. The amount of tracer-hydrogen increased in the latter half of fatigue lives for both steels, indicating damage accumulation prominently close to the final fracture. The amounts of tracer-hydrogen in fatigued specimens decreased by annealing at 473 K, indicating the vacancy-type nature of the lattice defects created before fracture. However, changes in the amount of tracer-hydrogen in the incubation stage were not simple, depending on the tested steel. Before an increase in the late stage of fatigue, the amount of tracer-hydrogen gradually decreased with fatigue cycles in PC steel, while the decrease was minimal in Si–Cr steel. The reason of the decrease and its dependence on steels is not definite, but reconfigurations or annihilation of dislocation structures during cyclic stressing were premised [58].

Similarly, lattice defects generated during delayed fracture tests were evaluated using tracer-hydrogen introduced into specimens subjected to fatigue cycles. Tracer-hydrogen was introduced into specimens interrupting loading and degassing at 303 K for 168 h at the unloaded state. Figure 7.19 [59] shows the amounts of tracer-hydrogen introduced to fine-grain 0.32% C martensitic steel specimens subjected to sustained loading in 20% NH_4SCN aqueous solution at 323 K. The applied stress was 60% or 80% of the tensile strength, and both levels were apparently within the elastic range.

In Fig. 7.19, the amount of tracer-hydrogen, i.e., hydrogen absorption capacity, initially decreased and then gradually increased with increasing loading time. In fractured specimens, the portions near the fracture surface showed substantially high tracer-hydrogen contents, as indicated by Δ and $\blacktriangle$ marks. The high values are due to concentrated strain near the fracture surface, likely associated with crack propagation, but the gradual increase before fracture is consistent with the strain-induced creation of vacancies and its concern with fracture. The initial decrease might be due to the reconfiguration of dislocations in martensite associated with hydrogen entry

Fig. 7.19 Amounts of tracer-hydrogen introduced to martensitic steel bar specimens subjected to sustained loading at 0.6 or 0.8 of the tensile strength in 20% NH_4SCN aqueous solution at 323 K (50 °C). Δ and $\blacktriangle$ denote fractured specimens (Doshida et al. [59]. Reprinted with permission from The Iron and Steel Institute, Japan)
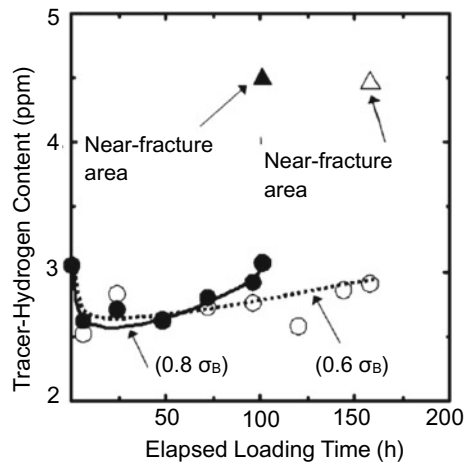
and loading. A similar initial decrease followed by a gradual increase in tracer-hydrogen content was also observed for a rotational bending fatigue test of high-strength steel [58]. Alterations of TDA profiles with increasing sustained-loading time are consistent with the formation of vacancy clusters, as described in Sect. 2.2.1 concerning Fig. 2.5 and Sect. 3.2 concerning Figs. 3.5 and 3.11.

Compositional dependence of hydrogen degradation in high-strength martensitic steel exhibiting IG fracture is presented in Figs. 7.6 and 7.7. The compositions of the steels were similar except Mn contents, and the slow-elongation rate tensile test was under simultaneous hydrogen charging [26]. A crucial issue concerning IG fracture is the involvement of plasticity in embrittlement. A useful tool to detect lattice defects is to utilize tracer-hydrogen, and the amount of absorbed tracer-hydrogen represents the densities of trap sites. Figure 7.20 [26] shows the amounts of hydrogen absorbed to saturation in specimens given various amounts of strain. The amounts for the three steels are almost the same when unstrained. On the other hand, a substantial increase by straining appeared more pronouncedly for higher manganese contents. As described in Figs. 3.2 and 3.10, TDA gives information about the nature of strain-induced defects.

Figure 7.21 [26] shows TDA curves of tracer-hydrogen introduced into three states of the 1.5% Mn specimens, i.e., unstrained, strained to 2%, and annealed at 523 K for 1 h after straining. The increase in the amounts of tracer-hydrogen totally disappeared by annealing the strained specimen at temperatures as low as 523 K, indicating that lattice defects that interact with tracer-hydrogen are vacancies rather than dislocations. Thus, the origin of the effect of Mn contents is reasonably ascribed to the density of strain-induced vacancies. Precipitation of carbides along martensite boundaries was present, but quantitative differences in microstructures that specify the three steels were not definite. Related degradations of tensile properties are described in Sect. 8.1.4 concerning Fig. 8.11

Positron annihilation spectroscopy (PAS), described in Sect. 3.2.2, is a more direct method to detect damage, particularly vacancies with large free volumes. PAS

Fig. 7.20 The amounts of hydrogen absorbed to saturation in specimens given various amounts of prestrain. The three martensitic steels with different Mn contents are used for Figs. 7.6 and 7.7 (Nagumo et al. [26])
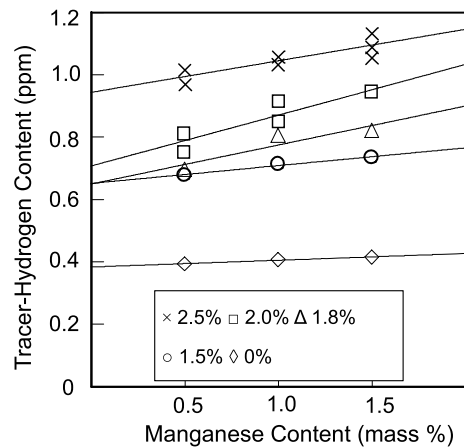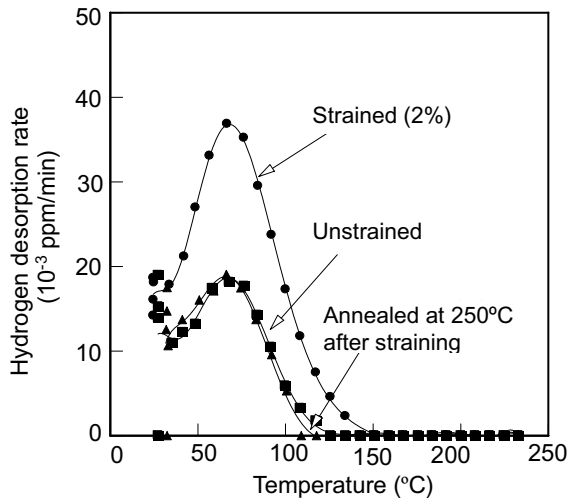
Fig. 7.21 Thermal desorption profiles of tracer-hydrogen introduced to 1.5% Mn steel specimens, unstrained, prestrained to 2%, and annealed at 250 °C (523 K) for 1 h after straining (Nagumo et al. [26])

was applied to identify the type of lattice defects generated during tensile straining of hydrogenated Type 304 steel. Figure 7.22 [13] shows the mean positron lifetimes τ_m of Type 304 and Type 316L steels given tensile strain with and without hydrogen charging to 30 mass ppm. Hydrogen charging enhanced the increase in τ_m with increasing strain. The strain-induced increase in τ_m implies the creation of lattice defects that have longer τ_m than the bulk. Successive isochronal annealing of strained materials showed a monotonic reduction in τ_m with increasing annealing temperatures [13].

The decrease in τ_m by annealing continued to temperatures as high as 1000 K, but the enhanced increase in τ_m by hydrogen disappeared by annealing at 573 K.

Fig. 7.22 Mean positron lifetimes of strained austenitic stainless steels: ◇: SUS304, ◆: H-charged SUS304, △: SUS316L, × : H-charged SUS316L (Hatano et al. [13])
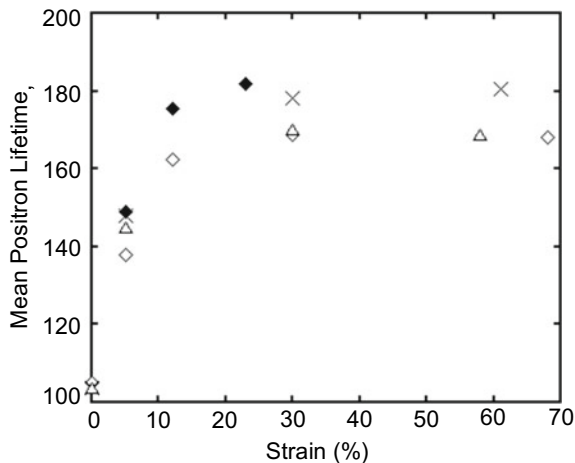
The annihilation temperature corresponds to vacancy clusters, and the difference in hydrogen effects between Type 304 and Type 316L is reasonable to ascribe to the creation and clustering of strain-induced vacancies. The results are consistent with PAS measurements for iron [60]. However, the observed τ_m is a weighted average of multiple lifetime components, as described in Sect. 3.2.2. The contributions of dislocations and vacancies to τ_m for iron deformed with and without hydrogen precharging are tabulated in Table 3.5. Deformation microstructures are further described in Sect. 8.3.4.

7.4.2 Effects of Stress History—Damage Accumulation

Hydrogen degradation manifests under various types of loading, and resultant mechanical properties are measures of degradation. Controlling factors of degradation differ by the type of loading, and the operating mechanism might not necessarily be identical. Structural components tolerate various stress histories during service. However, the damage produced in the early stages is carried over to the final fracture. In this section, some studies about the effects of stress histories on hydrogen degradation are presented.

In Sect. 6.1, the viable role of vacancy-type lattice defects in hydrogen degradation is presented for tensile tests of iron, cold-drawn eutectoid steel, and Inconel 625 alloy. Cyclic variations of applied stress promote failure at sustained-loading delayed fracture tests of martensitic steel as described in Sect. 6.4.3a. The degradation by cyclic prestressing implies the accumulation of strain-induced damage when the plasticity induced by prestressing is minor. Then, the effects of cyclic prestressing with and without hydrogen on tensile tests were examined for martensitic steel of 1433 MPa in tensile strength concerning the creation of damage [60]. Initially, the applied stress was cyclically varied in the range of 0.7 ± 0.1 of the tensile strength under hydrogen charging by immersing specimens in 20% NH_4SCN solution at 323 K. The specimens with and without hydrogen charging were denoted as [σ + H] and [σ], respectively. Degradation of tensile properties due to hydrogen was expressed in terms of the hydrogen embrittlement susceptibility (HES), defined as the ratio of the fracture strain of [σ + H] to that of [σ] specimens at following tensile tests.

Effects of cyclic prestressing on HES are shown in Fig. 7.23 [61] for increasing numbers of prestressing cycles at various strain rates. Cyclic prestressing enhances HES, i.e., hydrogen degradation, more pronouncedly by increasing the number of cycles and reducing the strain rates. Damage introduced by cyclic prestressing was then examined using hydrogen as the tracer. Tracer-hydrogen was introduced to saturation to cyclically prestressed specimens after exposing prestressed specimens at 323 K for 168 h to delete hydrogen present at the prestressing stage. External stress was not applied when introducing tracer-hydrogen under the same condition as the initial charging. The amounts of tracer-hydrogen increased with the number of stress cycles in both [σ] and [σ + H] specimens. The difference between [σ + H]

Fig. 7.23 Hydrogen
embrittlement susceptibility
(HES) on tensile tests of
martensitic steel specimens
applied cyclic prestressing at
various strain rates (Doshida
et al. [61])
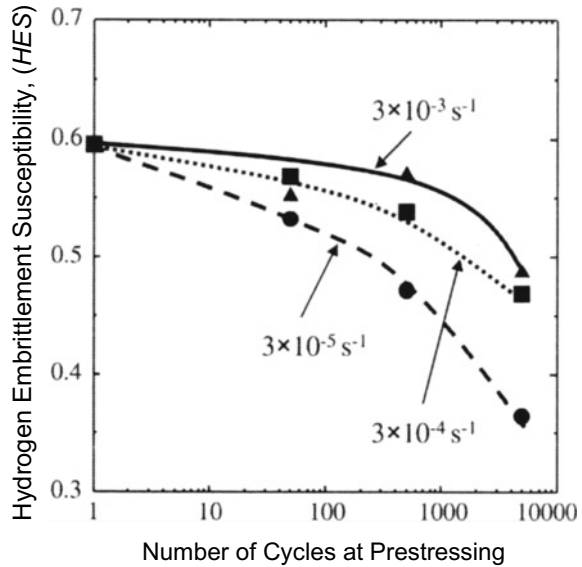
and $[\sigma]$ specimens was denoted as ΔC_H. It is a measure of the increased damage due to hydrogen. The amount of ΔC_H represents hydrogen effects on the strain-induced creation of defects at cyclic prestressing.

The magnitude of ΔC_H increased with cyclic stressing more pronouncedly with lower strain rates, as shown in Fig. 7.24 [61]. The increase in ΔC_H with decreasing strain rate is consistent with Fig. 6.4b in Sect. 6.1.1.2 for tensile tests. It indicates that cyclic stressing accumulates damage prior to the tensile tests. The tracer-hydrogen thermal desorption profiles showed a single peak centered at about 393 K, and ΔC_H humped the higher-temperature side of the TDA peak, implying vacancy clusters as described in Sect. 3.2.3.2. An approximately linear correspondence exists between HES and ΔC_H [60].

It supports the notion that the hydrogen-enhanced creation of damage causes degradation throughout the whole stage of plastic deformation. In Sect. 6.3.1, promoted fracture by hydrogen at rotational bending fatigue tests of high-strength Si–Cr steel is described, and the defect creation in the early stages of tests before the final fracture is shown in Fig. 6.18. Similarly, in delayed fracture, defects are accumulated in the incubation period, as shown in Fig. 7.19 for high-strength Si–Mn martensitic steel. The findings lead to the notion that stress histories play a crucial role in hydrogen degradation.

An experiment that demonstrated the effects of prefatigue on following sustained loading delayed fracture tests is shown in Fig. 7.25 [62] for the Si–Cr martensitic steel used for Fig. 6.16. Stress cycling (prefatigued) was applied by rotational bending for cycles about a half (Treat-A) of or close (Treat-B) to the fatigue life at the applied stress amplitude level of 640 MPa [62]. The two types of specimens were successively subjected to sustained-loading delayed fracture tests in 20% NH$_4$SCN

Fig. 7.24 Hydrogen enhancement of the strain-induced increase in the hydrogen absorption capacity, ΔC_H, on tensile tests of martensitic steel specimens after cyclic prestressing at various strain rates (Doshida et al. [61])
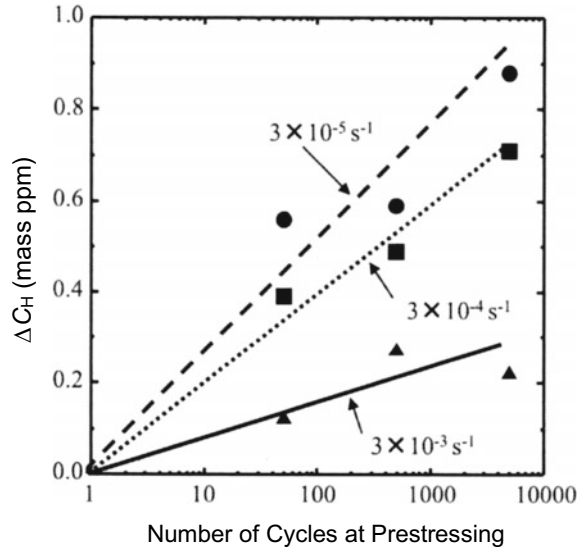
aqueous solution at 323 K. Specimens without prefatigue (Treat-N) were also tested for comparison. The fracture of specimens given prefatigue for cycles close to the fatigue life, Treat-B, occurred substantially earlier. However, annealing the fatigued specimens at a temperature as low as 473 K for 1 h reduced the degradation caused by prefatigue. The results indicate that damage accumulated during prefatigue plays a function in failure common to that created during sustained loading and that damage introduced by prefatigue is mostly vacancies without forming flaws such as voids and cracks.

Inversely, damage accumulated in sustained loading deteriorated tensile properties following the sustained loading [62]. Specimens of 5 mm in diameter of high-strength martensitic steel, 1433 MPa in tensile strength, were initially sustained-loaded at a constant stress of 80% of the tensile strength, apparently within the elastic range, for 96 h in 20% NH_4SCN aqueous solution at 323 K. After the sustained loading, hydrogen was completely removed at 303 K for 168 h, and then, some specimens were annealed at 473 K for 2 h. The two series of specimens are denoted as [H+ stress (96 h)] and [H + stress (96 h) + 200 °C], respectively. Also, specimens without sustained loading but annealed at 473 K were prepared with the notation of [non-stressed + 200 °C]. Stress–strain curves at tensile tests are shown in Fig. 7.26 [61]. It is to be noticed that a substantial degradation appeared for the [H+ stress (96 h)] series, although hydrogen was absent at the time of tensile testing. The almost complete recovery for the [H+ stress (96 h) + 200 °C] series indicates that vacancy-type defects, created during sustained loading without forming irreversible voids or cracks, cause the degradation.

Effects of environmental variations on delayed fracture, described in Sect. 6.4.3b, are similar to stress histories in respect of the damage accumulation. The stress history
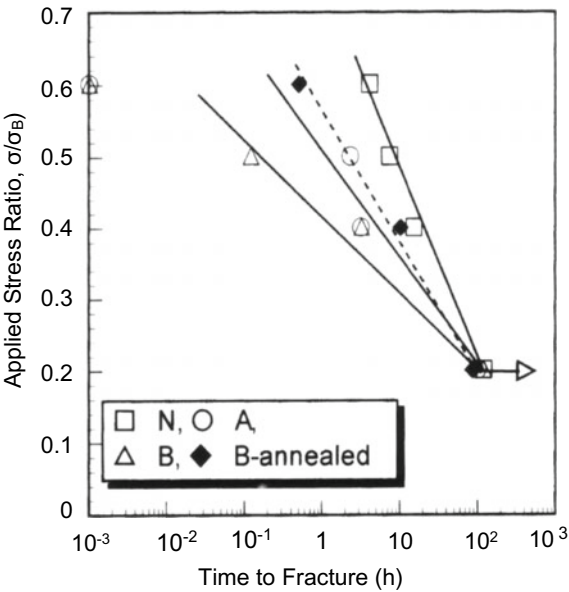
Fig. 7.25 Delayed fracture diagrams for prefatigued Si–Cr martensitic steel. □: N (without prefatigue), △ : B (prefatigued close to failure), ◆: B (annealed at 200 °C for 1 h after prefatigue), ○: A (prefatigued to about one half of fatigue life) (Nagumo et al. [62])
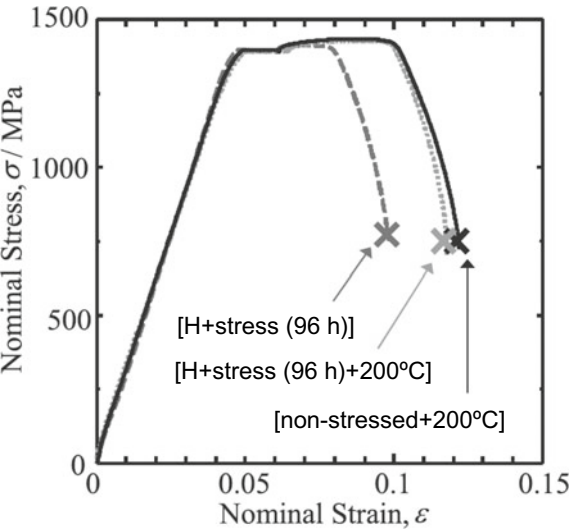

Fig. 7.26 Tensile curves of high-strength martensitic steel specimens. [H+ stress (96 h)]: Initially sustained-loaded in 20% NH₄SCN aqueous solution for 96 h at 50 °C (323 K), [H+ stress (96 h) + 200 °C]: Annealed at 200 °C (473 K) after sustained loading, [non-stressed + 200 °C]: Annealed at 200 °C (473 K) without sustained loading. All specimens are degassed at room temperature before tensile tests (Doshida et al. [61]. Reprinted with permission from The Iron and Steel Institute, Japan)

effects imply that the function of hydrogen in embrittlement must be examined over the entire fracture process, not merely at the final crack initiation and propagation stages. *The cumulative deterioration of material must be a crucial aspect of the function of hydrogen in embrittlement.*

References

1. F. Terasaki, T. Kawakami, A. Yoshikawa, N. Takano, Rév. Métall-CIT/Sci. Génie Matér. **95**, 1520–1529 (1998)
2. M.-J. Lii, X.-F. Chen, Y. Katz, W.W. Gerberich, Acta Metall. Mater. **38**, 2435–2453 (1990)
3. T.J. Marrow, M. Aindow, O. Prangnell, M. Strangwood, J.F. Knott, Acta Mater. **44**, 3125–3140 (1996)
4. F. Nakasato, I.M. Bernstein, Metall. Trans. A **9A**, 1317–1326 (1978)
5. M. Nagumo, K. Miyamoto, J. Jpn. Inst. Metals **45**, 1309–1317 (1981)
6. A.H. Cottrell, in *Dislocations and Plastic Flow in Crystals*, Sect. 14.6 (Oxford Press, London, 1961)
7. A.S. Tetelman, W.D. Robertson, Acta Metall. **11**, 415–426 (1963)
8. A.S. Tetelman, W.D. Robertson, Trans. Metall. Soc. AIME **224**, 775–783 (1962)
9. R. Gerber, I.M. Bernstein, A.W. Thompson, Scr. Metall. **10**, 341–345 (1976)
10. J.A. Gordon, J.P. Hirth, A.M. Kumar, N.E. Moody Jr., Metall. Trans. A **23A**, 1013–1020 (1992)
11. M. Nagumo, H. Yoshida, Y. Shimomura, T. Kadokura, Mater. Trans. **42**, 132–137 (2001)
12. S.P. Lynch, Acta Metall. **32**, 79–90 (1984)
13. M. Hatano, M. Fujinami, K. Arai, H. Fujii, M. Nagumo, Acta Mater. **67**, 342–353 (2014)
14. A. Shibata, H. Takahashi, N. Tsuji, ISIJ Int. **52**, 208–212 (2012)
15. Y.H. Kim, J.W. Morris Jr., Metall. Trans. A **14A**, 1883–1888 (1983)
16. Y. Shimomura, M. Nagumo, in *Environment-Induced Cracking of Materials: Chemistry, Mechanics and Mechanisms*, ed. by S.A. Shipilov, R.H. Jones, J.M. Olive, R.B. Rebak (Elsevier, Oxford, 2007), pp. 285–294
17. M.L. Martin, J.A. Fenske, G.S. Liu, P. Sofronis, I.M. Robertson, Acta Mater. **59**, 1601–1606 (2011)
18. M.L. Martin, I.M. Robertson, P. Sofronis, Acta Mater. **59**, 3680–3687 (2011)
19. A. Nagao, C.D. Smith, M. Dadfarnia, P. Sofronis, I.M. Robertson, Acta Mater. **60**, 5182–5189 (2012)
20. S.P. Lynch, Scr. Mater. **65**, 851–854 (2011)
21. T. Neeraj, R. Srinivasan, J. Li, Acta Mater. **60**, 5160–5171 (2012)
22. K. Yoshino, C.J. McMahon, Metall. Trans. **5**, 363–370 (1974)
23. W.W. Gerberich, T. Livne, X.-F. Chen, M. Kaczorowski, Metall. Trans. A **19A**, 1319–1334 (1988)
24. J. Kameda, Acta Metall. **34**, 1721–1735 (1986)
25. G.M. Ludtka, D.E. Laughlin, Metall. Trans. A **13A**, 411–425 (1982)
26. M. Nagumo, H. Matsuda, Phil. Mag. A **82**, 3415–3425 (2002)
27. M.L. Martin, B.P. Somerday, R.O. Ritchie, P. Sofronis, I.M. Robertson, Acta Mater. **60**, 2739–2745 (2012)
28. S. Wang, M.L. Martin, P. Sofronis, S. Ohnuki, N. Hashimoto, I.M. Robertson, Acta Mater. **69**, 275–282 (2014)
29. A. Shibata, Y. Momotani, T. Murata, T. Matsuoka, M. Tsuboi, N. Tsuji, Mater. Sci. Tech. **33**, 1524–1532 (2017)
30. C.D. Beachem, Metall. Trans. **3**, 437–451 (1972)
31. H. Yatabe, K. Yamada, E.R. de Los Rios, K.J. Miller: Fatigue Fract. Eng. Mater. Struct. **18**, 377–384 (1995)

32. M. Nagumo, T. Ishikawa, T. Endoh, Y. Inoue, Scr. Mater. **49**, 837–842 (2003)
33. A. Harada, K. Kusunoki, K. Moritani, K. Matsumoto, M. Hatano, Y. Horibe, Philos. Mag. Philos. Mag. Lett. **101**, 40–50 (2021)
34. M. Nagumo, T. Takahashi, Mater. Sci. Eng. **23**, 257–259 (1975)
35. D. Birenis, Y. Ogawa, H. Matsunaga, O. Takakuw, J. Yamabe, Ø. Prytz, A. Thøgersen, Acta Mater. **156**, 245–253 (2018)
36. Y. Ogawa, D. Birenis, H. Matsunaga, O. Takakuwa, J. Yamabe, Ø. Prytz, A. Thøgersen, Mater. Sci. Eng. A, **733**, 316–328 (2018)
37. Y. Ogawa, D. Birenis, H. Matsunaga, A. Thøgersen, Ø. Prytz, Scripta Mater. **140**, 13–17 (2017) Osamu Takakuwa e, Junichiro Yamabe
38. A. Setoyama, Y. Ogawa, M. Nakamura, Y. Tanaka, T. Chen, M. Koyama, H. Matsunaga: Int. J. Fatigue, https://doi.org/10.1016/j.ijfatigue.2022.107039.
39. D.G. Ulmer, C.J. Altstetter, Acta Metall. Mater. **39**, 1237–1248 (1991)
40. D.P. Abraham, C.J. Altstetter, Metall. Mater. Trans. A **26A**, 2859–2871 (1995)
41. Y. Murakami, T. Kanezaki, Y. Mine, Metall. Mater. Trans. A **41**, 2548–2562 (2010)
42. A. Inoue, Y. Hosoya, T. Masumoto, Trans. ISIJ **19**, 170–178 (1979)
43. P.J. Ferreira, I.M. Robertson, H.K. Birnbaum, Mater. Sci. Forum **207–209**, 93–96 (1996)
44. L. Vitos, J.-O. Nilsson, B. Johansson, Acta Mater. **54**, 3821–3826 (2006)
45. H. Tanaka, N. Hommma, S. Matsunaga, Y. Murakami, Trans Jpn. Soc. Mech. Eng. A **73**, 1358–1365 (2007)
46. H. Uyama, M. Nakashima, K. Morishige, Y. Mine, Y. Murakami, Fatigue and Fract. Eng. Mater. Struct. **29**, 1066–1074 (2006)
47. O.A. Onyewuenyi, J.P. Hirth, Metall. Trans. A **14A**, 259–269 (1983)
48. T.D. Lee, T. Goldenberg, J.P. Hirth, Metall. Trans. A **10A**, 439–448 (1979)
49. Y. Takahashi, M. Tanaka, K. Higashida, H. Noguchi, Scr. Mater. **61**, 145–148 (2009)
50. K. Okada, A. Shibata, W. Gong, N. Tsuji, Acta Mater. **225**, 117549 (2022)
51. H. Su, H. Toda, R. Masunaga, K. Shimizu, H. Gao, K. Sasaki, M.S. Bhuiyan, K. Uesugi, A. Takeuchi, Y. Watanabe, Acta Mater. **159**, 332–343 (2018)
52. F.A. Nichols, Acta Metall. **28**, 663–673 (1980)
53. O.A. Onyewuenyi, in *Hydrogen Degradation of Ferrous Alloys*, ed. by R.A. Oriani, J.P. Hirth, M. Smialowski (Noyes Pub., Park Ridge N.J., 1985), pp. 414–453
54. I.-G. Park, A.W. Thompson, Metall. Trans. A, **21A**, 465–477 (1990)
55. I.M. Bernstein, H.W. Wagenblast, J.L. Bomback, Metall. Trans. **2**, 2533–2534 (1972)
56. K. Kamachi, in *Report of Research Team on the Mechanism of Delayed Fracture* (Iron Steel Institute, Japan, Tokyo, 1975), pp. 93–111
57. K.A. Nibur, B.P. Somerday, D.K. Balch, C. San Marchi, Acta Mater. **57**, 3795–3809 (2009)
58. M. Nagumo, H. Shimura, T. Chaya, H. Hayashi, I. Ochiai, Mater. Sci. Eng. **A348**, 192–200 (2003)
59. T. Doshida, H. Suzuki, K. Takai, N. Oshima, T. Hirade, ISIJ Int. **52**, 198–207 (2012)
60. K. Sakaki, T. Kawase, M. Hirano, M. Mizuno, H. Araki, Y. Shirai, M. Nagumo, Scr. Mater. **55**, 1031–1034 (2006)
61. T. Doshida, M. Nakamura, H. Saito, T. Sawada, K. Takai, Acta Mater. **61**, 7755–7766 (2013)
62. M. Nagumo, S. Sekiguchi, H. Hayashi, K. Takai, Mater. Sci. Eng. **344A**, 86–91 (2003)